

Self-gravitating Filament Formation from Shocked Flows: Velocity Gradients across Filaments

Che-Yu Chen,¹★ Lee G. Mundy,² Eve C. Ostriker,³ Shaye Storm⁴ and Arnab Dhabal²

¹*Department of Astronomy, University of Virginia, Charlottesville 22904, VA, USA*

²*Department of Astronomy, University of Maryland, College Park 20742, MD, USA*

³*Department of Astrophysical Sciences, Princeton University, Princeton 08544, NJ, USA*

⁴*Harvard-Smithsonian Center for Astrophysics, Cambridge, MA 02138, USA*

Accepted XXX. Received YYY; in original form ZZZ

ABSTRACT

In typical environments of star-forming clouds, converging supersonic turbulence generates shock-compressed regions, and can create strongly-magnetized sheet-like layers. Numerical MHD simulations show that within these post-shock layers, dense filaments and embedded self-gravitating cores form via gathering material along the magnetic field lines. As a result of the preferred-direction mass collection, a velocity gradient perpendicular to the filament major axis is a common feature seen in simulations. We show that this prediction is in good agreement with recent observations from the CARMA Large Area Star Formation Survey (CLASSy), from which we identified several filaments with prominent velocity gradients perpendicular to their major axes. Highlighting a filament from the northwest part of Serpens South, we provide both qualitative and quantitative comparisons between simulation results and observational data. In particular, we show that the dimensionless ratio $C_v \equiv \Delta v_h^2 / (GM/L)$, where Δv_h is half of the observed perpendicular velocity difference across a filament, and M/L is the filament’s mass per unit length, can distinguish between filaments formed purely due to turbulent compression and those formed due to gravity-induced accretion. We conclude that the perpendicular velocity gradient observed in the Serpens South northwest filament can be caused by gravity-induced anisotropic accretion of material from a flattened layer. Using synthetic observations of our simulated filaments, we also propose that a density-selection effect may explain observed subfilaments (one filament breaking into two components in velocity space) as reported in [Dhabal et al. \(2018\)](#).

Key words: ISM: clouds – ISM: magnetic fields – magnetohydrodynamics (MHD) – stars: formation – turbulence

1 INTRODUCTION

Filaments are prevalent in observed star-forming clouds ([Schneider & Elmegreen 1979](#); [Bally et al. 1987](#); [Goldsmith et al. 2008](#)), and are generally considered to be connected with dense, star-forming cores ([André et al. 2010](#); [Könyves et al. 2010](#); [Polychroni et al. 2013](#)). Since the extensive studies completed with *Herschel* ([Miville-Deschênes et al. 2010](#); [Ward-Thompson et al. 2010](#)), a number of properties of observed filaments have been intensively studied including the density and temperature profiles ([Arzoumanian et al. 2011, 2019](#); [Juvela et al. 2012](#); [Palmeirim et al. 2013](#), or see [André](#)

[et al. 2014](#) for a review), the velocity sub-structures termed “fibers” ([Hacar et al. 2013](#)), and the relative orientation between filaments and magnetic fields as revealed by *Planck* ([Planck Collaboration Int. XXXV 2016](#)). In addition, molecular line observations with dense gas tracers have also been used to probe the detailed kinematics within individual filamentary systems ([Kirk et al. 2013](#); [Fernández-López et al. 2014](#); [Dhabal et al. 2018](#)).

In theoretical studies, filamentary structures appear in large-scale simulations investigating turbulence-induced cloud evolution either with or without magnetic fields and/or self-gravity ([Ostriker et al. 1999, 2001](#); [Klessen et al. 2004](#); [Jappsen et al. 2005](#); [Padoan et al. 2007](#); [Nakamura & Li 2008](#); [Federrath 2016](#)), and also in more idealized stud-

★ E-mail: cc6pg@virginia.edu

ies of gravitational/magnetic instabilities in sheet-like clouds (Ciolek & Basu 2006; Basu et al. 2009; Van Loo et al. 2014). While filamentary structures can arise from a variety of dynamical processes, the densest ones, which ultimately host the formation of stars, are likely to form in gas that has been strongly compressed by a converging, supersonic flows. Numerical studies of colliding flows which also include turbulence have indeed demonstrated the formation of filaments in post-shock layers and creation of embedded self-gravitating cores (Vázquez-Semadeni et al. 2007; Gong & Ostriker 2011; Chen & Ostriker 2014; Gong & Ostriker 2015). Observations of filament separation in clouds has also suggested that filaments form within shock-compressed sheets (Hartmann 2002).

As filaments are seen in a diversity of environments, and at a range of scales, they may have several different formation mechanisms. Filaments of cold gas in the warm ISM may occur as a result of thermal instability in combination with turbulent compression and shear (e.g., Audit & Hennebelle 2005; Piontek & Ostriker 2005; Heitsch et al. 2006; Vázquez-Semadeni et al. 2006; Inoue & Inutsuka 2009). Within entirely-molecular gas, filaments are commonly considered to be the products of direct compression of interstellar turbulence, or as part of the cloud-scale gravitational collapse (see e.g., Hennebelle & André 2013; Gómez & Vázquez-Semadeni 2014; Auddy et al. 2016). Though filaments are often seen to have velocity substructure in both observations and simulations (e.g. Hacar et al. 2013; Moeckel & Burkert 2015), the classical filament model of a static, self-gravitating, infinitely long cylinder (Ostriker 1964) is still widely adopted to interpret observation results (e.g. Johnstone & Bally 1999; Hatchell et al. 2005; Arzoumanian et al. 2011). Static filament models with non-zero external pressure are more realistic than filaments of infinite radius for comparison to real clouds (Fischera & Martin 2012). It is also possible to consider temporal evolution of self-gravitating cylinders in various limits (e.g. Inutsuka & Miyama 1992; Heitsch 2013b). However, the lack of symmetry in molecular clouds and their dynamic nature implies that filaments in general must form from gas structures that are not cylindrically symmetric (Heitsch 2013a), and signatures of the formation may be evident in the velocity fields around filaments. In particular, when filaments form via self-gravitating contraction in a shock-compressed dense layer, the velocity field surrounding the center of the forming filament will have converging-flow motions primarily in a plane containing the filament (Chen & Ostriker 2014, 2015; hereafter CO14, CO15).

In this paper, we describe the kinematic properties of forming filaments as obtained in numerical MHD simulations, and compare to kinematic features revealed in molecular line observations conducted by the Combined Array for Research in Millimeter-wave Astronomy (CARMA) towards nearby star-forming clouds, as part of the *CARMA Large Area Star Formation Survey* (CLASSy) project (Storm et al. 2014, 2016; Lee et al. 2014). Several filaments in the Perseus and Serpens Molecular Clouds show clear gradient across their major axes in line-of-sight velocity (Fernández-López et al. 2014; Dhabal et al. 2018), a signature feature of preferred-direction accretion described in CO14. In addition, the relatively narrow turbulent line widths at high angular resolution in Perseus and Serpens indicate that these

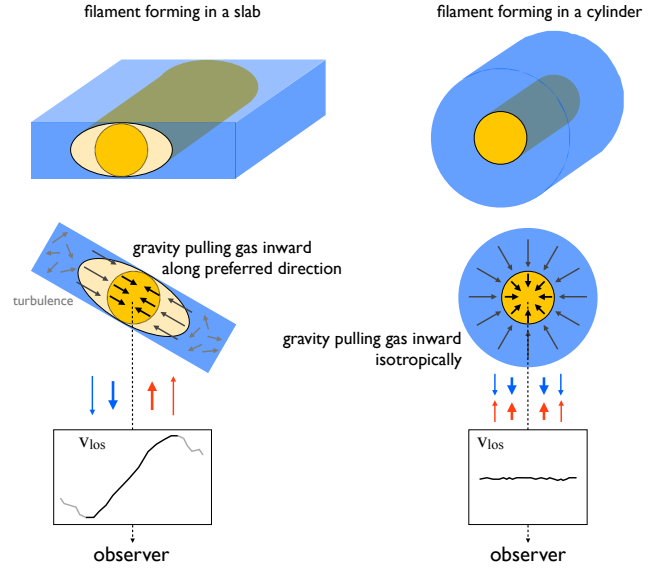


Figure 1. The “preferred-direction” filament formation versus isotropic gas flow. The observed velocity gradient across the filament indicates there is a preferred direction for gas flows near the filament (*left*). Filament formation within a compressed layer naturally exhibits convergent flow within the layer which appears as a local velocity gradient on the plane of the sky. In contrast, if the filament formation is cylindrically-symmetric, material is drawn in equally from around the cylinder and there is no gradient along the line-of-sight velocity, since the red-shifted and blue-shifted components are symmetric (*right*).

are flattened structures along the line of sight with depth ~ 0.3 pc (Lee et al. 2014; Storm et al. 2014), in agreement with the expected thickness of the post-shock layer created by converging flows (e.g. CO14, CO15). We therefore suggest that these observed filaments in Perseus and Serpens are forming via preferred-direction accretion within locally flat regions, which themselves may have been generated by large-scale shocks within each cloud.

The outline of this paper is as follows. We review and illustrate from simulation data our proposed model of filament formation within shocked layers in Section 2. In Section 3 we describe the numerical simulations we employ from CO14 and CO15, as well as how we characterize the filaments (Section 3.2). Section 3.3 presents discussions of the key properties of filaments identified in these simulations, including an evolutionary study and the quantitative measurements of gravity-induced velocity gradient. We provide a detailed comparison to observational data from CLASSy in Section 4, where we also discuss a possible origin of multiple velocity components within individual filaments (Section 4.3). We summarize our conclusions in Section 5.

2 FILAMENT FORMATION WITHIN FLAT LAYERS: KINEMATIC SIGNATURES

In simulations of large-scale supersonic converging flows, small-scale perturbation initiates local overdensities within the shock-compressed layer. In the case that the large-scale converging flow produces a shocked layer that becomes marginally self-gravitating, even small velocity per-

turbations would induce formation of overdense structures that start gravitationally pulling in material to form added filaments and dense cores. Such two-stage model for core formation in strongly magnetized layers is described in CO14 and CO15.

Since the perpendicular component of the velocity is mostly lost in transitioning through the shock, the gas velocity within the compressed layer is mostly parallel to the plane of the shock front. Therefore, if viewed from an angle not perfectly face-on to the post-shock layer, the line-of-sight velocity around a filament will have a gradient across its major axis. This “preferred-direction” filament formation process is illustrated in Figure 1. The gradient is initially due to the relatively weak, locally-converging velocity perturbation within the post-shock layer that is necessary to generate the seed of the filament. This proto-filament grows faster than the layer, and once it becomes overdense enough to be strongly self-gravitating, it draws in the denser infalling material from the post-shock layer which maintains and enlarges the velocity gradient.

Note that in the filament formation scenario described above, magnetic field is not required for filaments to show velocity gradients perpendicular to their major axes (see e.g. Fig. 2 of Gong & Ostriker 2011). However, in the presence of dynamically-important magnetic field, the preferred-direction mass accretion guided by magnetic field lines could enhance the detection of velocity gradients across filaments by regulating gas flows surrounding the filaments. Also note that, though the flows that produce filaments are primarily along magnetic fields, it is not necessary for filaments to be strictly perpendicular to the local magnetic field, because the loci of maximum density along each filament need not be exactly perpendicular to the magnetic field direction (see e.g. Figure 3 below).

We emphasize that our proposed model of filament formation differs from that described in Auddy et al. (2016), which considered filaments as ribbon-like structures that are the direct products from magnetic field-regulated turbulent compression. In our picture, the formation of filaments is a two-step process: a converging portion of a supersonic turbulent flow first compresses gas to form a dense layer (a two-dimensional structure), and then the one-dimensional, string-like filaments form within this locally-flat region via anisotropic gas accretion as shown in Figure 1. This filament formation scenario also differs from that investigated in Hennebelle & André (2013) and Gómez & Vázquez-Semadeni (2014), which formed filaments via the gravitational collapse of a molecular cloud as a whole. One would not expect to see velocity gradient across the major axis of the filament under such global contraction, which is more similar to the case shown in the right panel of Figure 1.

Figure 2 illustrates some examples of this kind of velocity gradients within filaments described above, from synthetic observations of model A5ID of CO14. The column density and the density-weighted line-of-sight velocity are projected along the direction that is 45° from the post-shock plane and 45° from the rough direction of the mean magnetic field in the layer (approximately along $\hat{\mathbf{x}}$), which is roughly perpendicular to the largest filaments (see the insert at bottom right on Figure 2). For closer comparison to observations using a dense-gas tracer (e.g. the CLASSy data discussed below in Section 4), we only include vox-

els from the computational output with number densities between $10^4 - 10^7 \text{ cm}^{-3}$. Figure 2 demonstrates that prominent velocity gradients across the filaments’ major axes are commonly seen in simulated star-forming regions generated by shocks, which could be an observable feature of filaments formed within a flattened layer.

However, gravity-induced anisotropic accretion is not the only way to produce a velocity gradient perpendicular to the filament’s major axis. Filaments formed from direct compression of local shocks could also show such velocity gradients. These filaments are likely confined by external ram pressure provided by the shock flows, which would result in a more significant velocity difference across the filament. Here, we propose that these two scenarios of filament formation could be easily distinguished quantitatively if the velocity difference across the filament and the mass per unit length of the filament are known.

For simplicity, we consider an idealized cylindrical filament with mass M and length L . For radial contraction induced by self-gravity, we have

$$\ddot{r} = -2 \frac{GM(r)/L}{r}. \quad (1)$$

This can be integrated to give (see e.g. Heitsch et al. 2009)

$$\frac{1}{2} \dot{r}^2 = 2G \ln\left(\frac{r_0}{r}\right) M(r)/L, \quad (2)$$

which represents the radial velocity of gas being pulled gravitationally from distance r_0 to r by the filament. The ratio r_0/r can be approximated as $r_0/r \sim \Sigma/\Sigma_0$ by considering the mass per unit length of the filament, $M/L = \Sigma \cdot r \sim \Sigma_0 \cdot r_0$, where Σ is the column density of the filament, and Σ_0 represents the average column density of the surrounding environment wherein the filament has formed. It has been shown in CO15 that $\Sigma/\Sigma_0 \sim 2 - 20$ for sufficiently advanced times such that the filament becomes prominent (see their Figure 6), which means the logarithm term in Equation (2), $\ln(r_0/r)$, can be considered as order of unity. Equation (2) therefore would yield

$$\dot{r}^2 \sim GM(r)/L \quad (3)$$

for gravitationally contracting filaments.

As discussed above, the velocity gradient across a filament may be either induced by the self-gravity of the filament, or may simply reflect supersonic turbulence of the cloud. To quantitatively distinguish between these two scenarios, we define a dimensionless coefficient C_v to compare the ratio between the kinetic energy of the flow transverse to the filament and the gravitational potential energy of the filament gas:

$$C_v \equiv \frac{\Delta v_h^2}{GM(r)/L}. \quad (4)$$

Here, Δv_h is half of the velocity difference across the filament out to a transverse distance r (on both sides), and $M(r)/L$ is the mass per unit length of the filament measured at the same distance from the spine as the Δv_h measurement. The value of C_v is suggestive of the origin of the velocity gradient. If $C_v \gg 1$, the local turbulence is much stronger than the filament’s self-gravity, and the filament is likely forming as a result of shock compression. If $C_v \lesssim 1$, the gravitational potential energy is comparable to the gas kinetic energy,

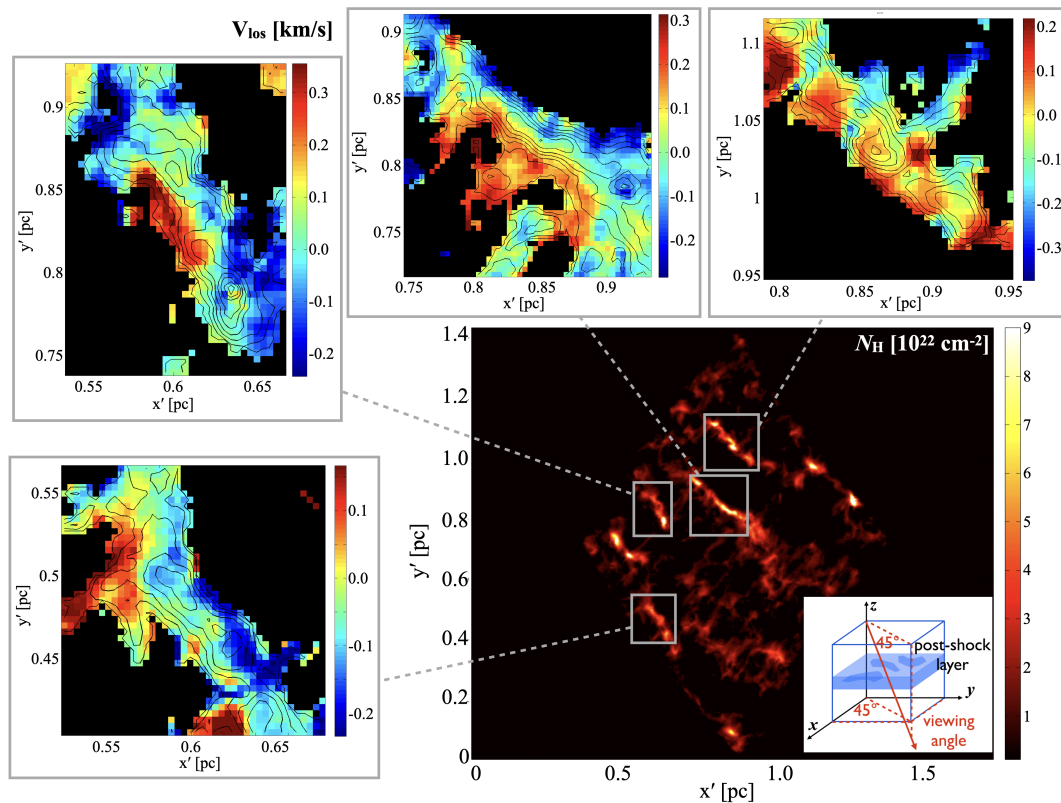


Figure 2. The kinematic features of filaments that form in self-gravitating converging turbulent flow simulations. In the example simulation from CO14, large-scale supersonic turbulence converges locally along the z -direction, forming a post-shock layer in the x - y plane (*insert, bottom-right*). When viewed from any direction (except perfectly edge-on), the integrated column density map (*bottom-right*) shows filamentary structures formed within the dense post-shock layer. Loci of four line-of-sight velocity maps are marked with gray boxes. A velocity gradient perpendicular to the major axis of each filament is a common feature for filaments formed within a dense layer when viewed at any angle except perfectly face-on.

which following Equations (2) or (3) suggests that the velocity structure is likely induced by the filament’s self-gravity. We would like to point out that filaments could in principle have $C_v \ll 1$ because of projection effects, or if a filament is at an early formation stage in our proposed scenario. Slowly re-expanding filaments could also have $C_v \ll 1$; however, we note that these filaments are shorter-lived and are less likely being seen in observations.

Below we provide examples and tests of our filament formation model using both numerical simulations and existing observation data.

3 FILAMENTS IN SIMULATIONS

3.1 Simulations

The simulations we use are reported in CO14, CO15 and summarized here. Those simulations, considering a magnetized shocked layer produced by plane-parallel converging flows, were conducted using the *Athena* MHD code (Stone et al. 2008), with box size $(1 \text{ pc})^3$ and resolutions $256^3 - 512^3$ (such that $\Delta x \approx 0.002 - 0.004 \text{ pc}$). In these simulations, box-scale supersonic inflows ($\mathcal{M} = 10$; modeling the largest-scale turbulence in a cloud) collides head to head along the z -axis of the simulation box, creating a flat post-shock region in

the x - y plane. The flow includes a local perturbed velocity field that follows the scaling law for turbulence in GMCs $\sigma_v(\ell) \propto \ell^{1/2}$ (with a Fourier power spectrum $v^2(k) \propto k^{-4}$; see Gong & Ostriker (2011)), with a largest scale of 1/2 of the box size. For simplicity, an isothermal equation of state with sound speed 0.2 km/s is adopted. We adopt model M10B10 from CO15 for our use in this work except in Figure 2, which uses model A5ID from CO14 to illustrate the kinematic feature because there are more separated filaments formed in this particular simulation.

The initial magnetic field in the simulation is set to be oblique to the shock on the $x - z$ plane with total magnitude $10 \mu\text{G}$. Within the post-shock layer, the magnetic field component parallel to the layer (B_x) is strongly enhanced by compression, while the perpendicular component (B_z) is not. The post-shock magnetic field is therefore relatively well-ordered, approximately along the x direction. Though the exact field strength depends on the angle between the initial magnetic field and the inflow, the post-shock magnetic pressure is approximately equal to the ram pressure in the inflow in the strong shock limit: $B_{\text{ps}}^2/(8\pi) \sim \rho_0 v_0^2$ (see CO14 and CO15). This applies when the post-shock region is dynamically dominated by the shock-amplified magnetic field.

As discussed in Section 2, to observe the “preferred-direction” filament formation as illustrated in Figure 1, the

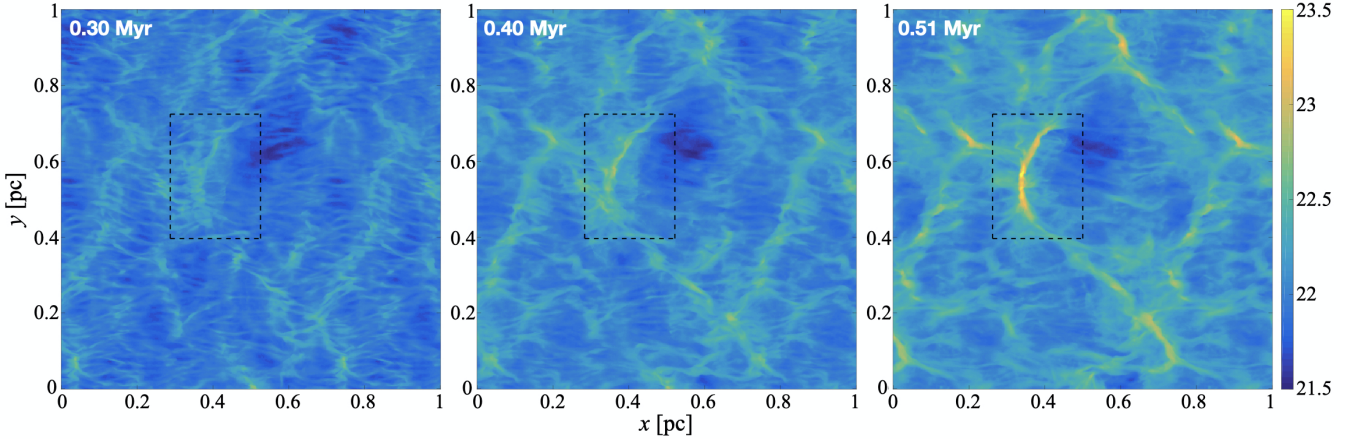


Figure 3. Snapshots of gas column density showing evolution to create filaments in model M10B10 from CO15. The post-shock magnetic field lies parallel to the \hat{x} direction. Gravity causes gas to flow along the magnetic field towards local density maxima, and over time filaments build up from accreted material. The inset box in dashed lines marks the region analyzed in Figure 4 below.

post-shock layer must have a non-zero relative angle with respect to the plane of sky (see e.g. Figure 2). Therefore in the analysis discussed below, the simulation box has been rotated by $\theta = 45^\circ$ around the y axis. We note that though this viewing angle affects the measured velocity difference across the filament (and therefore the value of C_v), it is not critical in our analysis as long as it is not the extreme cases ($\theta \sim 0^\circ$ or $\theta \sim 90^\circ$). Some discussions of the viewing angle effect are included in Section 4.3.

Figure 3 shows an example of the evolution of gas structures formed in the post-shock region (in column density) at 45° viewing angle; since the simulation box is periodic in the x direction, there are repeated patterns near the edge of the box. Filamentary structures become prominent at a time $\sim 0.3 - 0.5$ Myr after the initial collision of the convergent flows, with major (more massive) filaments aligned roughly perpendicular to the local magnetic field.¹ We can already see the footprints of anisotropic gas accretion onto the filaments from these sequential pc-scale maps; in the next section, we focus on the $\sim 0.3 \times 0.2$ pc² zoom-in region around the main filament of this simulation (marked by the dashed-line box in Figure 3) for quantitative analysis.

3.2 Characterizing Filaments

As filaments are effectively projected structures in 2D in observations, we use the column density map to define filaments. For the main filament in this simulation and within the zoom-in region from Figure 3, we picked the two ends of the filament that we want to analyze, and then marked the “spine” of the filament by finding the maximum column density at each row of y . We then calculate the distance to the spine for each pixel, and consider only pixels at distance $d_{\text{fila}} < 0.05$ pc to the spine in our following analysis. These are shown in the top row of Figure 4, where we over-plotted

the spine of the filament and the ± 0.05 pc area on the column density map of the zoom-in region from Figure 3. Note that this selection of d_{fila} takes the recent *Herschel* results (that typical filament width ~ 0.1 pc) into consideration, and also (based on the results) is large enough to cover the velocity gradients across the filaments formed in this simulation.²

We can therefore plot the column density and line-of-sight velocity profiles of the filament with respect to offset from the spine, which are shown in the second row (column density profile) and fourth row (velocity profile) of Figure 4. Using the column density profile, we chose to define the filament width in a similar way as the full width at half maximum (FWHM); i.e. we label the edges of the filament based on where the column density (in log space) drops to 50% of (maximum–background) above the background. Here, the “background” column density is defined as the minimum value of the column density profile, which is calculated within $\pm d_{\text{fila}}$ from the spine. These filament boundaries are marked as vertical dashed lines in both the column density and line-of-sight velocity profiles in Figure 4, with the filament width labeled on the top-right corner of the column density plot (second row) at each time frame. We note that, though our method of characterizing filaments and the choices of parameter values may seem artificial, it does not affect our results on filament kinematics significantly, since we focus on relative comparisons among evolutionary sequences instead of exact measurements of physical properties at a specific time. In addition, as most of those filament parameters (mass per unit length, width, etc.) are highly uncertain in observations, we are only making order-of-magnitude comparisons, and therefore the detailed modeling of specific filaments is not the main focus here.

¹ There are also thin, hair-like sub-filaments (or striations) that seem to follow the direction of magnetic field; these are not our main focus in this study. For further discussions regarding these field-aligned striations, see Chen et al. (2017).

² In fact, note that the simulation considered here (model M10B10 from CO15) is an ideal MHD simulation, and is therefore scale-free, which means it can be easily rescaled to represent a different physical scale (see e.g. King et al. 2018). This is why we do not discuss, or compare with those measured in observations, the width of simulated filaments here.

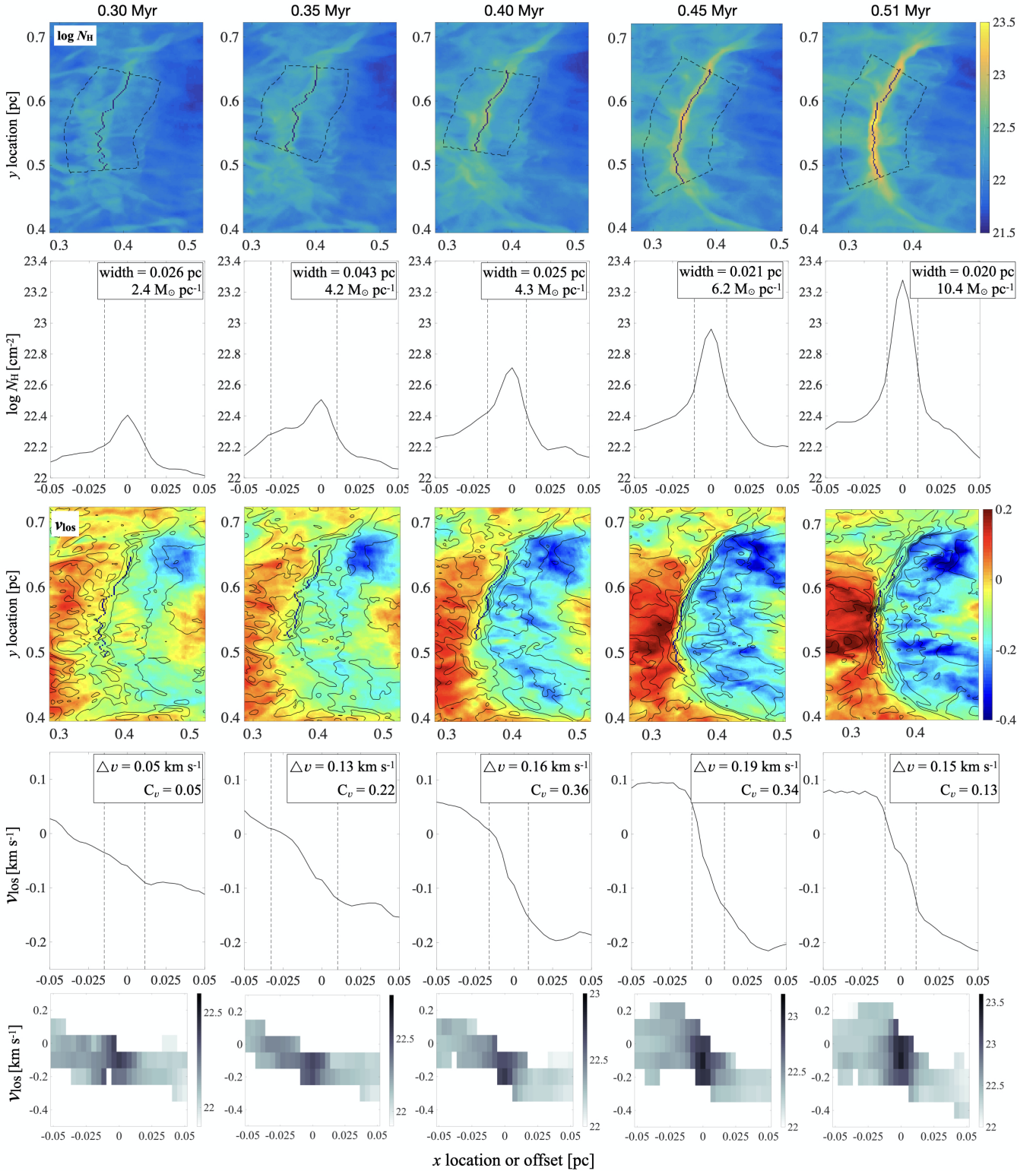


Figure 4. The evolution of a sample filament (marked in dashed box in Figure 3), showing the N_{H} column density map (*top row*, in log scale) and profile (*second row*), the line-of-sight velocity (*third row*, in km s^{-1}) and profile (*fourth row*), and the converted position-velocity diagram (*bottom row*). The dashed regions in the column density maps mark the 0.05 pc radius from the spine (black dots) that are considered in the profile plots and PV diagrams. The boundaries of each filament (as defined in Section 3.2) are marked by vertical dashed lines in either the column density or velocity profile plots. The filament width, mass per unit length, velocity difference across the filament, and the C_v coefficient are also noted in those panels.

3.3 Filament Kinematics and Evolution

The mass per unit length of the filament can be derived by integrating filament column density over the filament width, which is labeled on the top-right corner of each column density profile in Figure 4 (second row). Not surprisingly, though the filament width does not vary much over the ~ 0.2 Myr time coverage of Figure 4, the mass per unit length increases by almost a factor of 5. The nearly-constant filament width could be a hint that the filament is already self-gravitating at $\sim 0.3 - 0.4$ Myr, because otherwise the filament width should grow when materials flow in and accumulate, thus increase with its mass. This agrees with our filament formation model described in Section 2, that the post-shock layer was already at the verge of gravitational instability when the filament started forming.

Using the column density-defined filament boundaries, we calculated the velocity difference Δv across the filament and the corresponding C_v coefficient, both labeled on the top-right corner of the velocity profiles in Figure 4 (fourth row). Combining with the maps of density-weighted average of line-of-sight velocity in Figure 4 (third row), we see clear evidence of gravity-induced accretion onto this filament. At ~ 0.30 Myr after the shock compression (the first time frame of Figure 4), the right-hand-side of the filament does not show clear accretion flows onto the filament.³ This is also reflected in the relatively-gradual slope of the velocity profile and small Δv (0.05 km s^{-1}). As the filament becomes more and more massive ($0.35 - 0.40$ Myr), inward movements towards the filament spine start to emerge on the right-hand-side of the filament. This acceleration of gas can be seen on the velocity profile plot that v_{los} becomes more negative at positive offsets, and the increasing velocity difference across the filament ($\Delta v = 0.16 \text{ km s}^{-1}$ at 0.40 Myr).

Interestingly, at the time frame 0.45 Myr, the gas motion and the filament self-gravity seem to reach a balance, as the gas velocity on the left-hand-side of the filament (but outside the filament boundary) remains roughly constant (see the velocity profile plot on the fourth row of Figure 4). Though we cannot say the same for the right-hand-side (the side with positive offsets) of the filament, when comparing the velocity profiles at $t = 0.45$ Myr and 0.51 Myr (the last two columns in Figure 4) we see that the right-hand-side gas velocity did not change much over time, indicating that a rough balance between gas motion and the filament's self-gravity has also been reached. We note that the last time frame, $t = 0.51$ Myr, in Figure 4 marks the onset of gravitational collapse of the dense core within the filament;⁴ this is reflected on the most central part of the velocity profile, where a transition from a smooth slope (as in $t = 0.45$ Myr) to a relatively flat curve (i.e. constant velocity) happens. This flat region could be a result of radial collapse of the filament.

The evolution of velocity structure during the forma-

tion of the filament can be summarized by the position-velocity (PV) diagrams shown in Figure 4 (last row). We clearly see that the distribution of gas in the velocity space is initially flat (small Δv ; $t = 0.30$ Myr), and the slope becomes steeper and steeper when the filament accretes more material, forming a bright hub at the center of the PV space ($t = 0.35 - 0.45$ Myr). After ~ 0.45 Myr, the balance between the filament's self-gravity and surrounding gas motion is reached, and therefore the maximum gas speed on each side of the filament varies little over time. More interestingly, at $t = 0.51$ Myr we see the PV distribution of intermediate-density gas extends towards the reference velocity (i.e. the velocity of the filament spine at offset = 0) and is less concentrated (spreads out to larger offsets), indicating the end of gravity-induced accretion of gas.

Finally, as discussed in Section 2, we calculated the dimensionless coefficient C_v as a quantitative estimate of the relative importance between gas kinetic energy and the filament's self-gravity. The value of C_v at each evolutionary step is provided on the top-right corner of the velocity profile in Figure 4 (fourth row). One can immediately note that $C_v \sim 0.1 - 0.3$ over the forming process of this filament, which demonstrates that the filament's self-gravity is playing a critical role in shaping the velocity profile around this filament.

4 FILAMENTS IN OBSERVATIONS

Prominent velocity gradients perpendicular to the filament major axes have been observed in observations, in both a filamentary infrared dark cloud (Beuther et al. 2015) and nearby star-forming regions (Palmeirim et al. 2013; Shimajiri et al. 2018). Those velocity features are, in a number of cases, very similar to what is seen in our preferred-direction mass accretion model when the filaments form within locally-flat regions (see Section 2). Here, we highlight a filament from the northwest part of the Serpens South Molecular Cloud to conduct quantitative analysis and compare with our numerical models.

4.1 Observations: CLASSy and CLASSy-II

The data we use are from the CARMA Large Area Star Formation Survey (CLASSy) and follow-up observations (referred as CLASSy-II). The CLASSy project spectrally imaged N_2H^+ , HCO^+ , and HCN ($J = 1 \rightarrow 0$) over 800 square arcminutes of the Serpens and Perseus Molecular Clouds, focusing on the NGC 1333, Barnard 1, and L1451 regions within Perseus, and the Main and South regions of Serpens (Storm et al. 2014, 2016; Lee et al. 2014). The observational details are given in those papers; relevant points for this discussion are that the velocity resolution was $\sim 0.16 \text{ km s}^{-1}$ and the spatial resolution was $\sim 7.6''$.

From the CLASSy sample, several filaments with velocity gradients across the filament width are detected (see e.g. Fernández-López et al. 2014); the CLASSy-II project (Dhabal et al. 2018) followed up five filaments detected in CLASSy samples to further investigate the kinematics of filamentary structures. As a test of whether the observed velocity features arise from a chemical effect, CLASSy-II adopted optically thin dense gas tracers H^{13}CO^+ and H^{13}CN

³ Apparently, the local turbulence at the left-hand-side of the filament happens to be originally strong enough and pushing gas towards the filament, which could be the reason of the formation of the “seed” of this filament in the first place.

⁴ As described in CO14 and CO15, we define the onset of gravitational collapse of a dense core as when its maximum density reaches $\gtrsim 10^7 \text{ cm}^{-3}$.

that were not included in CLASSy. More details about the CLASSy-II observations can be found in [Dhabal et al. \(2018\)](#).

4.2 The Serpens South NW (SSNW) Filament

In this work, we consider the N_2H^+ data from CLASSy and the H^{13}CO^+ data from CLASSy-II of the Serpens South northwest (SSNW) filament as a real-life example of our filament formation model. The location of SSNW filament (northwest of the Serpens South hub) is marked by the white box in the left-most panel of Figure 5, which shows the *Herschel* column density map of the Serpens South region. Note that there are other filaments in the Serpens South region showing similar velocity gradients ([Fernández-López et al. 2014](#); [Dhabal et al. 2018](#)), but those filaments are closer to the bright, massive Serpens South hub of star formation, making their structure and kinematics more complex. The SSNW filament is more isolated and away from the main star formation activity in the region, and therefore is ideal for our investigation here.

The upper-half of the middle and right four panels of Figure 5 summarizes the results from CLASSy N_2H^+ and CLASSy-II H^{13}CO^+ observations towards the SSNW filament, showing the integrated intensity (left) and best-fit centroid velocity offset of the gas (right), which have been reported in [Dhabal et al. \(2018\)](#) (see their Fig. 2). The velocity offsets are calculated with respect to the median velocity of the gas within the filament boundaries (see below), $\langle v_{\text{fila}} \rangle = 7.53$ and 7.54 km s^{-1} for N_2H^+ and H^{13}CO^+ , respectively. It is clear that the line-of-sight velocity of gas within the SSNW filament gradually shifts from $\sim +0.4 \text{ km s}^{-1}$ on the southwest edge to $\sim -0.1 \text{ km s}^{-1}$ on the northeast side in both N_2H^+ and H^{13}CO^+ emissions. This velocity gradient is better illustrated in Figure 6, which shows the PV diagrams of the SSNW filament from both N_2H^+ (left) and H^{13}CO^+ (right) emissions. Here, the offset is calculated with respect to the spine of the filament (dashed straight line in the intensity maps; see below for definition). Both N_2H^+ and H^{13}CO^+ emission distributions show steep slopes in the PV space; as discussed in the simulations in Section 3.3, this is a clear evidence of velocity gradient across the filament.

Since neither of the N_2H^+ and H^{13}CO^+ data successfully recovered a continuous spine of the SSNW filament (peak intensity at the center of the filament along its major axis), our method discussed in Section 3.2 is not applicable here. We therefore hand-picked the spine of the SSNW filament by eye, which is marked as a straight dashed line in the upper panels of Figure 5. All pixels with $> 2\sigma$ signals in the centroid velocity map (regions within the dashed contour in the integrated intensity map) are included in calculating the radial profiles of integrated intensity and centroid velocity offset, which are plotted in the bottom-half of the four-panel set in Figure 5 for both N_2H^+ (middle set) and H^{13}CO^+ (right set). The filament boundaries are defined using the N_2H^+ emission at where the intensity drops below half of the peak value.⁵ Note that because of the higher noise level

of the H^{13}CO^+ data, the filament boundaries in H^{13}CO^+ uses those defined in N_2H^+ data. The two boundaries are marked by vertical dashed lines in the intensity and velocity profiles in Figure 5; the width for the SSNW filament is therefore $D_{\text{SSNW}} \approx 0.08 \text{ pc}$.

To quantify the magnitude of the velocity gradient across the SSNW filament, we linearly fit the velocity profiles within the filament boundaries, and measure the velocity difference between the two ends of the fit, which is overplotted on the velocity profiles in Figure 5 (dotted lines). The velocity difference across a width of 0.08 pc in the SSNW filament is 0.27 and 0.31 km s^{-1} for N_2H^+ and H^{13}CO^+ , respectively.

From the *Herschel* column density map of the Serpens South cloud, we estimated an average column density along the SSNW filament to be $N_{\text{H}} \sim 2.1 \times 10^{22} \text{ cm}^{-2}$. Considering the filament width $D_{\text{SSNW}} \approx 0.08 \text{ pc}$, this yields the mass per unit length $M/L = N_{\text{H}} m_{\text{H}} \cdot D_{\text{SSNW}} \approx 14 M_{\odot} \text{ pc}^{-1}$. Therefore, the C_v coefficient (see Equation (4)) for the SSNW filament is about 0.36 . The fact that $C_v < 1$ in the SSNW filament indicates that the observed velocity gradient perpendicular to the filament could be induced by its self-gravity. In addition, this C_v values agree with those derived from our simulated filaments for times when the filament is becoming prominent (see Figure 4). We therefore propose that the SSNW filament is formed within a locally-flat region by gravitationally accreting material anisotropically.

4.3 Subfilaments in PV Diagram: Multiple Structures or Density Selection Effect?

[Dhabal et al. \(2018\)](#) found in their data an interesting feature that some filaments seem to break into two subfilaments in PV space (see e.g. their Fig. 9 and 12), with velocity difference $\sim 0.5\text{--}1.0 \text{ km s}^{-1}$. Multiple velocity components have also been observed in the L1495/B213 filaments in Taurus ([Hacar et al. 2013](#)), and have been interpreted as subfilaments which are either created from filament fragmentations ([Tafalla & Hacar 2015](#)) or are going to collide to form more massive filaments ([Smith et al. 2016](#)). Here, as an extension of our filament formation model, we provide an alternative explanation to the subfilaments reported in [Dhabal et al. \(2018\)](#): density selection effect.

Considering the nature of molecule excitation, each molecular line is prominent over a certain range of gas density. This means that for a given molecular line, it may not trace the entire filament all the way from the outer part to the central spine, which could have density (or column density) enhancement as large as an order of magnitude (see e.g. Figure 4). A similar argument has been discussed in [Clarke et al. \(2018\)](#), who used synthetic C^{18}O observations of filaments formed in turbulent simulations to show that C^{18}O emission could be dominated by the outer envelopes of the central, overdense regions of the filaments and thus show multiple velocity components in the spectra.

Though detailed chemical modeling and radiative transfer calculation is beyond the scope of this paper, a simple experiment using our simulated filament (Figure 4) demonstrates this *density selection effect*, which is illustrated in

⁵ This definition is different from that adopted in our simulated filament, which takes the “background” into consideration (see Section 3.2). Since both N_2H^+ and H^{13}CO^+ are considered as

dense gas tracers, they should not be sensitive to lower density background gas.

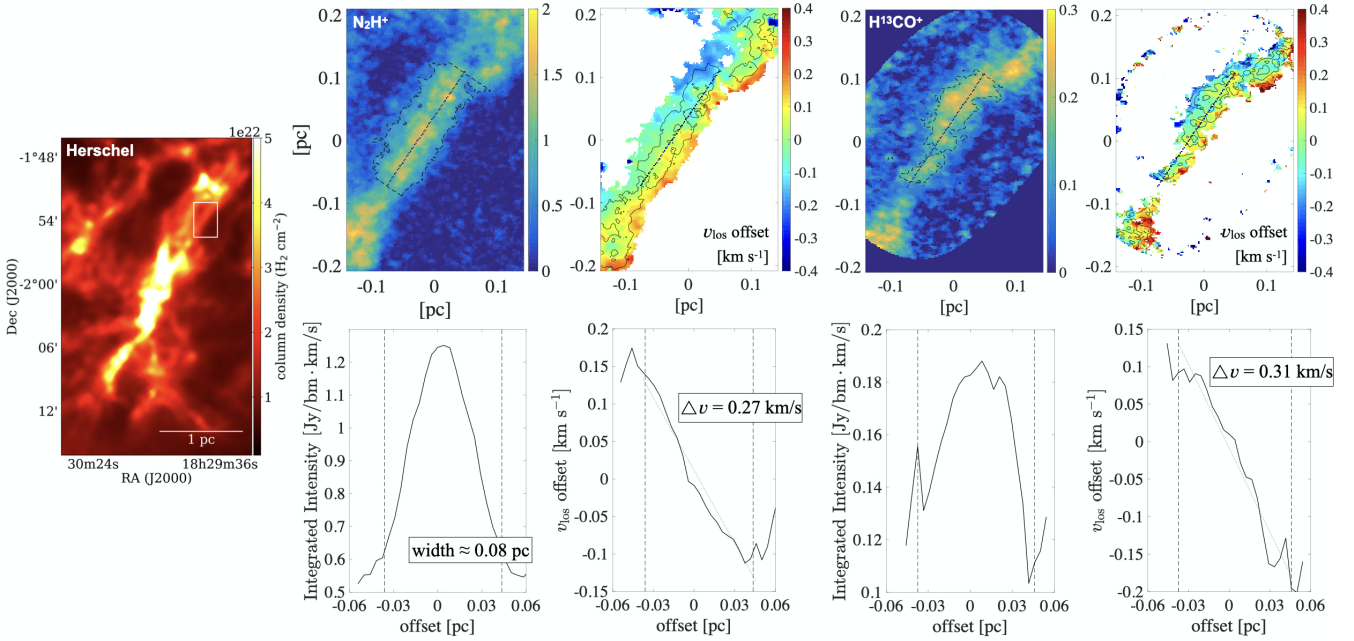


Figure 5. *Left:* The *Herschel* column density map of Serpens South region, with the location of the Serpens South NW filament marked by white box. *Middle set of four panels:* The N_2H^+ integrated intensity in $\text{Jy beam}^{-1}\text{km s}^{-1}$ (*top left*) and line-of-sight velocity offset (*top right*, with integrated intensity contours) maps of the SSNW filament from CLASSy, with the corresponding spatial profiles (*bottom sub-panels*) measured with respect to the spine of the filament (*dashed straight line in the upper panels*). *Right set of four panels:* Similar to the middle four panels, but for H^{13}CO^+ data from CLASSy-II. Both data sets are clipped at 2σ (see [Dhabal et al. 2018](#)). The width of the filaments (in both N_2H^+ and H^{13}CO^+) are defined by the FWHM of the N_2H^+ integrated intensity because of the slightly higher noise in H^{13}CO^+ data. The velocity differences measured from both tracers at the same width are also labeled on the velocity profile plots.

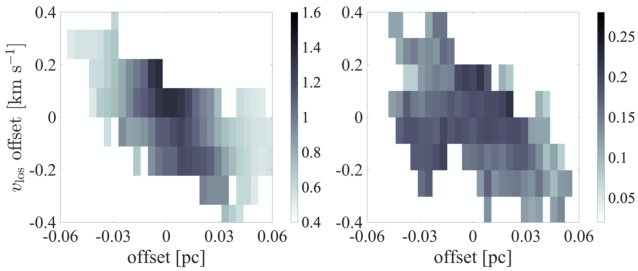


Figure 6. The PV diagrams of the SSNW filament, from CLASSy N_2H^+ data (*left*) and CLASSy-II H^{13}CO^+ data (*right*).

Figure 7. The first column of Figure 7 shows the same column density map and PV diagram from the last column of Figure 4, which represents the “ideal” situation when every voxel in the filament is contributing equally to the integrated column density. These voxels have volume density range $n_{\text{H}} \sim 10^{3.5} - 10^8 \text{ cm}^{-3}$. With the same viewing angle (45° from the normal of the locally-flat shock-compressed layer where the filament formed), the third column of Figure 7 shows the integrated column density map and PV diagram of the filament with a density cutoff: only voxels with gas density within the range $n_{\text{H}} = 10^{3.5} - 10^5 \text{ cm}^{-3}$ are included in calculating column density. Two separated components

can be clearly seen in the resulting PV diagram,⁶ with velocity difference $\sim 0.3 \text{ km s}^{-1}$. This nicely reproduces the subfilaments in PV space observed by [Dhabal et al. \(2018\)](#).

However, one may ask why subfilaments in PV space are not always seen in observations, like the SSNW filament discussed in the previous section (see e.g. Figure 6). In addition to chemical dependence of molecular line emission on gas properties, we argue that the viewing angle could also be critical in finding these subfilaments. In Figure 7 we present the column density maps and PV diagrams of the same filament with the same density cutoff, but from two additional inclination angles of the filament-forming layer with respect to the plane of sky, 30° (second column) and 60° (fourth column), to compare with the fiducial case 45° (first and third columns). Obviously, the separation between the two components in the PV space becomes less prominent when the inclination angle is large (i.e. when the layer is close to edge-on), and one can hardly distinguish the two “subfilaments” in PV space for the case of inclination angle = 60° . This can be easily understood as gas contents from the two sides of the filament overlap along the line of sight.

⁶ Note that for cases with density cutoffs, the spine of the filament and the region considered in the PV diagram are derived from the original simulation data without density cutoff, because with density cutoffs the central part of the filament no longer corresponds to local maxima in column density, and therefore it is impossible to define the spine.

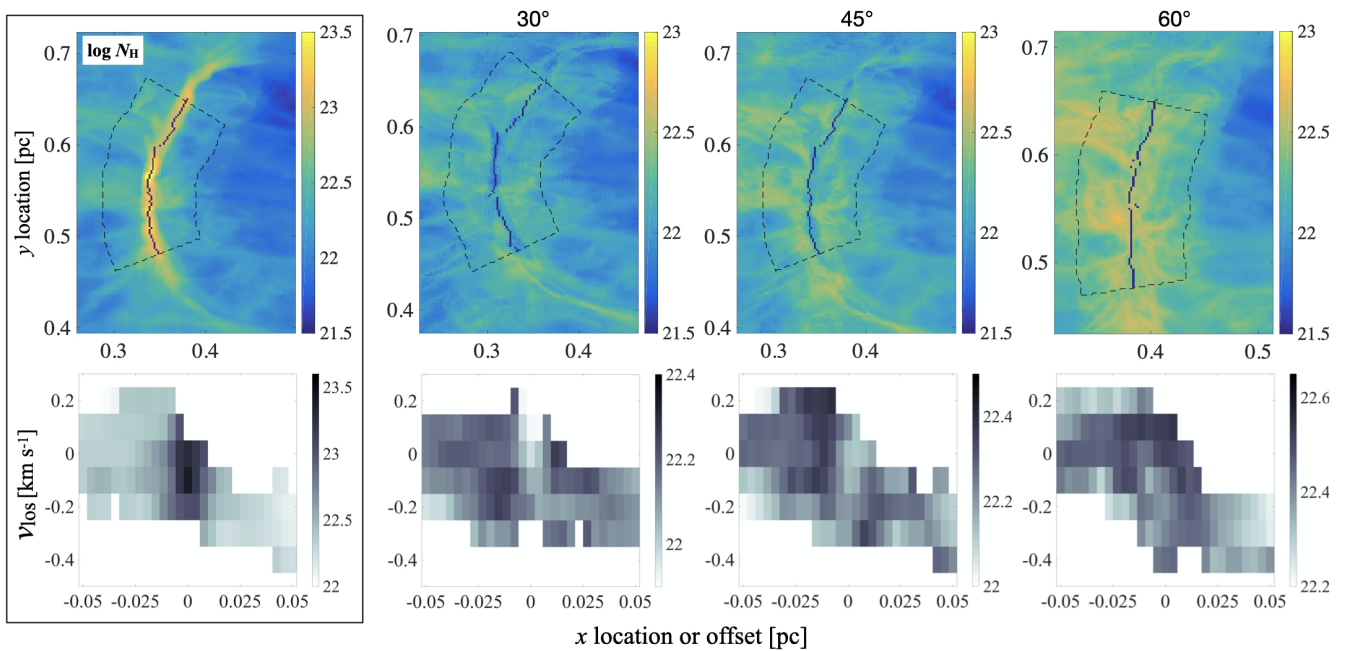


Figure 7. Illustration of the density selection effect at various viewing angle. The first column represents the reference case, which is from the last column of Figure 4; i.e. considering all cells with volume density with $10^{3.5} - 10^8 \text{ cm}^{-3}$ with viewing angle 45° . Columns 2 – 4 show the same filament viewed at different angles, and including only cells within the narrower density range $10^{3.5} - 10^5 \text{ cm}^{-3}$. *Top row:* N_{H} column density map (in log scale). *Bottom row:* PV diagram along the filament spine (*black lines* in the top row) for gas within the 0.05 pc radius (*dashed regions* in the top row). The subfilaments can be clearly seen in the PV diagram for some viewing angles, which is simply caused by the missing high-density gas near the filament spine (small offset from the filament).

We would also like to point out that another feature of these density selection effect-induced subfilaments is that the spine of the filament is sometimes missing or less obvious in the integrated emission map, because there are not enough voxels along the line of sight at the central part of the filament that are within the required density range to contribute to the integration. In observations, this represents the case when the gas density around the filament spine is too high to emit the specific molecular line in consideration. This feature can be actually seen in some filaments reported in [Dhabal et al. \(2018\)](#) that have multiple components in PV space, like the Serpens South E filament (their Fig. 3) and the NGC 1333 SE filament (their Fig. 6).

Note that we do not claim that density selection effect is the reason for all observed subfilaments (or fibers) in velocity space, even though it does appear that these subfilaments are more common in moderate-density tracers (e.g., C^{18}O) than high-density tracers (e.g., N_2H^+). Future high-resolution continuum observations will be the key to revealing the unbiased gas structure of these filaments with multiple velocity components.

5 SUMMARY

In this paper, we combine kinematics of observed and simulated dense gas structures to provide evidence for a model in which gas filaments form via in-plane flows parallel to the magnetic field in shock-compressed layers. CLASSy data towards Perseus and Serpens Molecular Clouds demonstrated prominent velocity gradients transverse to the filament ma-

ior axis, a feature of the preferred-direction accretion model of filament formation, as shown in numerical simulations of [CO14](#) and [CO15](#). The quantitative comparison between kinetic and gravitational energy also suggests that the observed velocity gradients are induced by the filament self-gravity.

Our main conclusions are as follows:

(i) We quantitatively examine a scenario to form dense, star-forming filaments within locally-flat gas layers compressed by supersonic turbulence within a molecular cloud. In the case that the shock is strong enough to compress gas to be almost self-gravitating, local velocity perturbation within the shocked layer can lead to the filamentary structure by creating seeds that grow via gravitational collection of material. Within the layer, the gravity-induced accretion flows onto the forming filament are preferably parallel to the layer, which results in the kinetic feature of linear velocity gradient across the filament when viewed from any direction except face-on (Figure 1). This feature is commonly seen in numerical simulations ([CO14](#), [CO15](#)) considering convergent flows that compress gas and form post-shock layers wherein filaments and prestellar cores develop (Figure 2).

(ii) To demonstrate that the velocity gradient perpendicular to the major axis of a filament seen in our simulations is induced by the filament self-gravity, we follow the time evolution of a forming filament from one of our simulations (Figure 4). The fact that the velocity gradient becomes more prominent with the filament unit mass (mass per unit length) supports our model of the origin of such velocity gradient. In addition, by quantitatively calculating the ra-

tio between gas kinetic energy and filament gravitational energy C_v (Equation (4)), we show that the self-gravity of the filament is indeed strong enough to induce such velocity structure (Section 3.3).

(iii) We test our model on a filament in the Serpens South northwest region (SSNW filament), which was firstly observed by CLASSy and later followed-up by CLASSy-II (Dhabal et al. 2018). Both the CLASSy N_2H^+ and CLASSy-II $H^{13}CO^+$ data of the SSNW filament show velocity profiles in good agreement with our filament formation model very well, and with $C_v \sim 0.3$ the filament self-gravity is definitely responsible for the observed velocity gradient across the SSNW filament (Figure 5).

(iv) As an extension of our filament formation model, we propose that the multiple components in PV space within an individual filament, as reported in Dhabal et al. (2018), could be due to density selection effect. Instead of being real structures, these separated “subfilaments” may simply reflect the fact that the central zone of the filament is too dense to emit certain molecular lines that are used to trace the outer part of the filament. We demonstrate this effect by adopting a simple density cutoff on synthetic observations toward one of our simulated filaments, and we note that this effect is dependent on the viewing angle with respect to the locally-flat, filament-forming layer (Figure 7).

ACKNOWLEDGEMENTS

We thank the referee for a very helpful report. C.-Y. C. is grateful for the support from NSF grant AST-1815784. The work of E.C.O. was supported by grant 510940 from the Simons Foundation. CLASSy was supported by NSF AST-1139998 (University of Maryland) and NSF AST-1139950 (University of Illinois). Support for CARMA construction was derived from the Gordon and Betty Moore Foundation, the Kenneth T. and Eileen L. Norris Foundation, the James S. McDonnell Foundation, the Associates of the California Institute of Technology, the University of Chicago, the states of Illinois, California, and Maryland, and the National Science Foundation.

REFERENCES

André, P., Men’shchikov, A., Bontemps, S., et al. 2010, *A&A*, 518, L102
 André, P., Di Francesco, J., Ward-Thompson, D., et al. 2014, in *Protostars and Planets VI*, ed. H. Beuther, et al. (Tucson, AZ: Univ. Arizona Press), 27
 Arzoumanian, D., André, P., Didelon, P., et al. 2011, *A&A*, 529, L6
 Arzoumanian, D., André, P., Könyves, V., et al. 2019, *A&A*, 621, A42
 Auddy, S., Basu, S., & Kudoh, T. 2016, *ApJ*, 831, 46
 Audit, E., & Hennebelle, P. 2005, *A&A*, 433, 1
 Bally, J., Langer, W. D., Stark, A. A., & Wilson, R. W. 1987, *ApJ*, 312, L45
 Basu, S., Ciolek, G. E., & Wurster, J. 2009b, *NewA*, 14, 221
 Beuther, H., Ragan, S. E., Johnston, K., et al. 2015, *A&A*, 584, A67
 Chen, C.-Y., & Ostriker, E. C. 2014, *ApJ*, 785, 69
 Chen, C.-Y., & Ostriker, E. C. 2015, *ApJ*, 810, 126

Chen, C.-Y., Li, Z.-Y., King, P. K., & Fissel, L. M. 2017, *ApJ*, 847, 140
 Clarke, S. D., Whitworth, A. P., Spowage, R. L., et al. 2018, *MNRAS*, 479, 1722
 Ciolek, G. E., & Basu, S. 2006, *ApJ*, 652, 442
 Dhabal, A., Mundy, L. G., Rizzo, M. J., Storm, S., & Teuben, P. 2018, *ApJ*, 853, 169
 Dhabal, A., Mundy, L. G., Chen, C.-Y., et al. 2019, *ApJ*, 876, 108
 Federrath, C. 2016, *Monthly Notices of the Royal Astronomical Society*, 457, 375
 Fernández-López, M., Arce, H. G., Looney, L., et al. 2014, *ApJ*, 790, L19
 Fischera, J., & Martin, P. G. 2012, *A&A*, 542, A77
 Goldsmith, P. F., Heyer, M., Narayanan, G., et al. 2008, *ApJ*, 680, 428
 Gómez, G. C., & Vázquez-Semadeni, E. 2014, *ApJ*, 791, 124
 Gong, H., & Ostriker, E. C. 2011, *ApJ*, 729, 120
 Gong, M., & Ostriker, E. C. 2015, *ApJ*, 806, 31
 Hacar, A., Tafalla, M., Kauffmann, J., & Kovács, A. 2013, *A&A*, 554, A55
 Hartmann, L. 2002, *ApJ*, 578, 914
 Hatchell, J., Richer, J. S., Fuller, G. A., et al. 2005, *A&A*, 440, 151
 Heitsch, F. 2013, *ApJ*, 769, 115
 Heitsch, F. 2013, *ApJ*, 776, 62
 Heitsch, F., Ballesteros-Paredes, J., & Hartmann, L. 2009, *ApJ*, 704, 1735
 Heitsch, F., Slyz, A. D., Devriendt, J. E. G., et al. 2006, *ApJ*, 648, 1052
 Hennebelle, P., & André, P. 2013, *A&A*, 560, A68
 Inoue, T., & Inutsuka, S.-ichiro. 2009, *ApJ*, 704, 161
 Inutsuka, S.-I., & Miyama, S. M. 1992, *ApJ*, 388, 392
 Jappsen, A.-K., Klessen, R. S., Larson, R. B., Li, Y., & Mac Low, M.-M. 2005, *A&A*, 435, 611
 Johnstone, D., & Bally, J. 1999, *ApJ*, 510, L49
 Juvela, M., Ristorcelli, I., Pagani, L., et al. 2012, *A&A*, 541, A12
 Kainulainen, J., Hacar, A., Alves, J., et al. 2015, arXiv:1507.03742
 Klessen, R. S., Ballesteros-Paredes, J., Li, Y., & Mac Low, M.-M. 2004, *The Formation and Evolution of Massive Young Star Clusters*, 322, 299
 King, P. K., Fissel, L. M., Chen, C.-Y., & Li, Z.-Y. 2018, *MNRAS*, 474, 5122
 Kirk, H., Myers, P. C., Bourke, T. L., et al. 2013, *ApJ*, 766, 115
 Könyves, V., André, P., Men’shchikov, A., et al. 2010, *A&A*, 518, L106
 Lee, K. I., Fernández-López, M., Storm, S., et al. 2014, *ApJ*, 797, 76
 Miville-Deschênes, M.-A., Martin, P. G., Abergel, A., et al. 2010, *A&A*, 518, L104
 Moeckel, N., & Burkert, A. 2015, *ApJ*, 807, 67
 Nakamura, F., & Li, Z.-Y. 2008, *ApJ*, 687, 354
 Ostriker, J. 1964, *ApJ*, 140, 1056
 Ostriker, E. C., Gammie, C. F., & Stone, J. M. 1999, *ApJ*, 513, 259
 Ostriker, E. C., Stone, J. M., & Gammie, C. F. 2001, *ApJ*, 546, 980
 Padoan, P., Juvela, M., Goodman, A. A., et al. 2001, *ApJ*, 553, 227
 Padoan, P., Nordlund, Å., Kritsuk, A. G., Norman, M. L., & Li, P. S. 2007, *ApJ*, 661, 972
 Palmeirim, P., André, P., Kirk, J., et al. 2013, *A&A*, 550, A38
 Panopoulou, G. V., Tassis, K., Goldsmith, P. F., & Heyer, M. H. 2014, *MNRAS*, 444, 2507
 Piontek, R. A., & Ostriker, E. C. 2005, *ApJ*, 629, 849
 Planck Collaboration Int. XXXV. 2016, *A&A*, 586, A138
 Polychroni, D., Schisano, E., Elia, D., et al. 2013, *ApJ*, 777, L33
 Schneider, S., & Elmegreen, B. G. 1979, *ApJS*, 41, 87

- Shimajiri, Y., Andre, P., Palmeirim, P., et al. 2018, arXiv e-prints , arXiv:1811.06240.
- Smith, R. J., Glover, S. C. O., Klessen, R. S., & Fuller, G. A. 2016, MNRAS, 455, 3640
- Stone, J. M., Gardiner, T. A., Teuben, P., Hawley, J. F., & Simon, J. B. 2008, ApJS, 178, 137
- Storm, S., Mundy, L. G., Fernández-López, M., et al. 2014, ApJ, 794, 165
- Storm, S., Mundy, L. G., Lee, K. I., et al. 2016, ApJ, 830, 127
- Tafalla, M., & Hacar, A. 2015, A&A, 574, A104
- Van Loo, S., Keto, E., & Zhang, Q. 2014, ApJ, 789, 37
- Vázquez-Semadeni, E., Gómez, G. C., Jappsen, A. K., et al. 2007, ApJ, 657, 870
- Vázquez-Semadeni, E., Ryu, D., Passot, T., et al. 2006, ApJ, 643, 245
- Ward-Thompson, D., Kirk, J. M., André, P., et al. 2010, A&A, 518, L92

This paper has been typeset from a $\text{\TeX}/\text{\LaTeX}$ file prepared by the author.